J. Fluid Mech. (2019), *vol.* 879, *pp.* 579–603. © Cambridge University Press 2019
doi:10.1017/jfm.2019.666

Laminar–turbulent coexistence in annular Couette flow

Kohei Kunii[1], Takahiro Ishida[1,‡], Yohann Duguet[2] and Takahiro Tsukahara[1,†]

[1]Department of Mechanical Engineering, Tokyo University of Science, Chiba 278-8510, Japan

[2]LIMSI-CNRS, Université Paris-Sud, Université Paris-Saclay, F-91405 Orsay, France

(Received 25 December 2018; revised 8 August 2019; accepted 9 August 2019; first published online 1 October 2019)

Annular Couette flow is the flow between two coaxial cylinders driven by the axial translation of the inner cylinder. It is investigated using direct numerical simulation in long domains, with an emphasis on the laminar–turbulent coexistence regime found for marginally low values of the Reynolds number. Three distinct flow regimes are demonstrated as the radius ratio η is decreased from 0.8 to 0.5 and finally to 0.1. The high-η regime features helically shaped turbulent patches coexisting with laminar flow, as in planar shear flows. The moderate-η regime does not feature any marked laminar–turbulent coexistence. In an effort to discard confinement effects, proper patterning is, however, recovered by artificially extending the azimuthal span beyond 2π. Eventually, the low-η regime features localised turbulent structures different from the puffs commonly encountered in transitional pipe flow. In this new coexistence regime, turbulent fluctuations are surprisingly short-ranged. Implications are discussed in terms of phase transition and critical scaling.

Key words: turbulent transition, pattern formation

1. Introduction

Most wall-bounded shear flows possess a linearly stable base flow for parameters where turbulence can also be observed. This is particularly true near the onset of turbulence, i.e. near the smallest Reynolds number Re_g, 'g' for global, where turbulence is sustained. There is no contradiction between linear stability of the laminar base flow and the existence of a turbulent regime, since the latter can be reached from well-chosen finite-amplitude perturbations to the base flow (Orszag 1971; Schmid & Henningson 2001). Such turbulent flows are called subcritical, and there is no general method for identifying the value of Re_g. A large number of studies have demonstrated that turbulent regimes near Re_g are intermittent in space and time. At every instant in time they consist of trains of localised coherent structures such as turbulent puffs in pipe flow (Wygnanski & Champagne 1973; Wygnanski, Sokolov & Friedman 1975; Bandyopadhyay 1986; Barkley *et al.* 2015) and turbulent stripes in

† Email address for correspondence: tsuka@rs.tus.ac.jp

‡ Present address: Japan Aerospace Exploration Agency, Tokyo 182-8522, Japan.

https://doi.org/10.1017/jfm.2019.666 Published online by Cambridge University Press

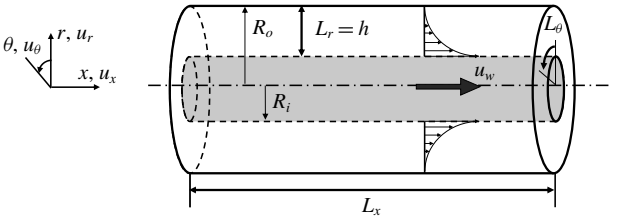


FIGURE 1. Configuration of aCf, with notations.

planar shear flows such as plane Couette flow (pCf) or plane Poiseuille flow (Prigent *et al.* 2002; Barkley & Tuckerman 2005; Tsukahara *et al.* 2005, 2010*a*; Fukudome & Iida 2012; Seki & Matsubara 2012).

A turbulent puff is a turbulent region localised in the axial direction of a pipe. A mechanism for the self-sustenance of this coherent structure has been identified by Shimizu & Kida (2009). However puffs do not persist indefinitely. As demonstrated by Hof *et al.* (2006), puffs have finite lifetimes as long as they keep their localisation. The onset Reynolds number Re_g is determined for the case of pipe flow as the value of Re at which the decay rate and proliferation rate exactly balance each other (Avila *et al.* 2011), i.e. 2040 ± 10 when Re is based on the flow rate and the pipe diameter.

Turbulent stripes are large-scale coherent structures emerging spontaneously near Re_g in a variety of planar wall-bounded flows such as pCf with or without rotation (Barkley & Tuckerman 2007; Tsukahara *et al.* 2010*a*; Duguet, Schlatter & Henningson 2010*a*; Tsukahara, Tillmark & Alfredsson 2010*b*; Brethouwer, Duguet & Schlatter 2012). They display obliqueness with respect to the mean flow direction, explained by the robust presence of oblique large-scale flows near the laminar–turbulent interfaces (Duguet & Schlatter 2013). The onset Reynolds number of pCf is estimated as $Re_g \approx 324 \pm 1$ using the classical definition of Re, from either experimental lifetime measurements (Bottin *et al.* 1998) or numerical decay experiments (Duguet *et al.* 2010*a*). Such structures were initially reported in counter-rotating regimes of Taylor–Couette flow (TCf) (Coles 1965; Prigent *et al.* 2002) and are not specific to perfectly planar geometries.

Whereas the coherent structures and the associated mean flows near Re_g for pipe flow can be described as one-dimensional, patterning in pCf is more genuinely two-dimensional. Establishing universal links between all the different sustained coherent structures (puffs, stripes) in such flows is an ambitious task. By noting that these coherent structures are (turbulent) steady states, one can borrow from bifurcation theories the concept of continuation, i.e. a continuous deformation from one flow case to another one, hoping that there is indeed at least one path in parameter space which continuously links one type of solution (here stripes) to the other one (puffs). If such a path exists then puffs and stripes can be considered members of a unique family of subcritical flows. Continuation methods have shown to be useful for the tracking of nonlinear steady states from one model problem to another. The first such instance was considered by Nagata (1990) who deformed tertiary solutions of TCf into non-trivial steady states of pCf. In the same spirit, Faisst & Eckhardt (2000) suggested a criterion to assess whether and when the curvature of TCf can be considered geometrically negligible.

In this article, we focus on a new candidate flow for continuation between pipe flow puffs and plane Couette stripes: annular Couette flow (aCf). This refers to the flow

https://doi.org/10.1017/jfm.2019.666 Published online by Cambridge University Press

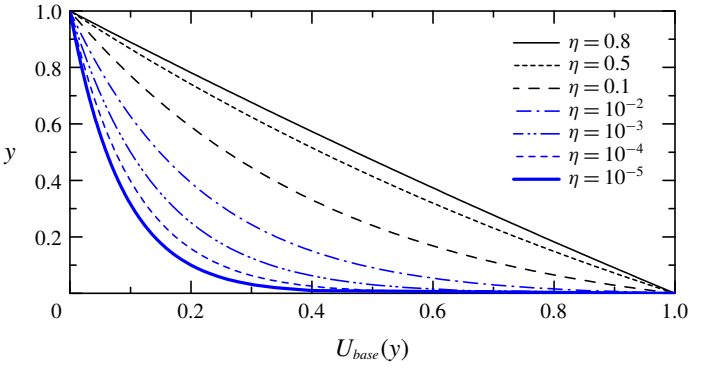


FIGURE 2. (Colour online) Laminar velocity profiles of aCf at several radius ratios. The values of η investigated in this article ($\eta = 0.8$, 0.5 and 0.1) are the three topmost curves (black online), while smaller values of η down to 10^{-5} are displayed using a clearer font (blue online). See § 2.1 for the definition of y.

between two infinitely long coaxial cylinders, driven by the axial translation of the inner rod with constant velocity $u_w > 0$. A sketch is displayed in figure 1. This flow is an idealised academic configuration inspired by thread-annular flows (Frei, Lüscher & Wintermantel 2000; Walton 2003, 2004, 2005; Webber 2008), for which large-scale coherent structures can limit the degree of homogeneity of the processed material. The main non-dimensional geometric parameter in aCf is the radius ratio $\eta = R_i/R_o$ (where R_i and R_o denote, respectively, the inner radius and outer radius). The radius difference, $h = R_o - R_i$, represents the gap between the two cylinders. As $\eta \to 1$, the wall curvature vanishes and the flow is asymptotically equivalent to pCf. At the other end, for $\eta \to 0$, the geometry does not become a cylindrical pipe because of the presence of the inner rod (associated with no slip). There is hence no possible continuation from aCf to pipe flow. Besides the difference in topology, the velocity distributions of pipe flow and aCf in the vanishing η limit strongly differ. This is readily seen by analysing the analytical laminar solutions shown in figure 2. For $\eta \to 1$ the profile clearly tends uniformly towards the centrosymmetric linear profile of pCf, whereas for $\eta \to 0$ the wall shear is located at the inner rod only, unlike pipe flow for which the shear is located at the outer boundary. A similar conclusion is expected for turbulent regimes but deserves a full quantitative study. The Reynolds number is defined as $Re = u_w h/4\nu$, where ν is the kinematic viscosity of the fluid. That definition is consistent with the pCf limit as η approaches 1.

A number of stability investigations have focused on the linear stability of the base flow as a function of η and Re. According to Gittler (1993), aCf is linearly stable against axisymmetric perturbations for $\eta > 0.1415$, while it becomes unstable at finite but very large Reynolds numbers ($Re > 10^6$) for $\eta < 0.1415$. Liu & Liu (2012) demonstrated the possibility for large non-modal growth of perturbations in the linearly stable regimes for most values of η and for values of Re much below the linear stability threshold. By considering non-axisymmetric perturbations and tracking numerically exact nonlinear travelling waves, Deguchi & Nagata (2011) determined the values of Re_g of 255.4, 256.6 and 288.6 for $\eta = 1^-$, 0.5 and 0.1, respectively. To our knowledge, no study has tracked turbulent coherent structures for fixed η all the way towards their extinction at Re_g.

https://doi.org/10.1017/jfm.2019.666 Published online by Cambridge University Press

It is the goal of the present paper to describe the distinct representative regimes of localised turbulence in aCf near Re_g. The mechanisms that can take aCf away from pCf for decreasing η are twofold: either azimuthal confinement prevents large-scale coherent structures from forming, or the wall curvature is such that the coherent structures themselves change form. These two mechanisms, though both linked to finite η, are different. We take inspiration from a cousin of aCf, namely annular Poiseuille flow (aPf), the flow occurring in the same geometry, yet with a non-moving inner rod and a pressure gradient applied against the axial direction. The different transitional regimes of aPf were described by Ishida, Duguet & Tsukahara (2016). Three types of coherent structures were identified depending on the value of η, all sketched in figure 3: helical stripes for η close to but below unity, straight puffs for low enough η and an intermediate state occurring near $\eta \approx 0.3$ in the form of a helical puff, i.e. a helical stripe of finite streamwise extent. Ishida, Duguet & Tsukahara (2017) performed a statistical analysis of the transition from puffs to stripes as η is varied, by investigating statistically the large-scale flows present at the laminar–turbulent interfaces. They revealed a statistical cross-over from straight puffs (figure 3*c*) to oblique laminar–turbulent interfaces (figure 3*b*), for radius ratios $\eta \approx 0.3$–0.4, where the flow consists of a spatially disordered mixture of helical and straight puffs. The main mechanism breaking the helical stripes of aPf is essentially azimuthal confinement: by noting that the length scale of interest is the annular gap width h, and by expressing all lengths in units of h, 'large-scale' flows can only be accommodated inside the gap for η close enough to unity. The geometry common to aCf and aPf leads to the expectation that transitional structures occurring in aCf are similar to those found in aPf. To this end we have chosen to focus on the transitional regimes occurring for the same values of $\eta = 0.8$, 0.5 and 0.1. For each case, we report whether or not turbulent stripes form as in pCf. In the absence of stripes, the mechanical reason for it, either azimuthal confinement or wall curvature, will be analysed. As will be described throughout the paper, the planar picture is valid for large $\eta \approx 1$, where the flow stays similar to pCf, but it breaks down for lower $\eta \leqslant 0.5$.

The present paper is structured as follows. Section 2 contains the governing equations and a description of the numerical tools. In § 3, the intermittent regimes are described for three different values of $\eta = 0.8$, 0.5 and 0.1 in decreasing order, with a focus on whether the flow patterns are influenced by the azimuthal confinement or not. Section 4 contains temporal statistics of the flow field as well as measures of intermittency. Finally the universal features of transitional aCf are discussed in § 5.

2. Governing equations and numerical methods

2.1. *Governing equations*

We consider an incompressible Newtonian fluid flow between two coaxial cylinders. The outer cylinder of radius R_o is fixed whereas the inner cylinder of radius R_i moves in the axial direction x with velocity $u_w > 0$. The gap has size $h = R_o - R_i$. The quantities h and u_w are used to non-dimensionalise the governing equations. The flow configuration is sketched in figure 1. The non-dimensional coordinates r and θ are, where necessary, converted respectively into $y = r - r_i$ and $z = r\theta$, where $r_i \leqslant r \leqslant r_o$, with $r_i = R_i/h$ and $r_o = R_o/h$. The non-dimensional velocity field $\boldsymbol{u} \equiv (u_x, u_r, u_\theta)$ in cylindrical coordinates and the pressure field are governed by the incompressible Navier–Stokes equations:

$$\boldsymbol{\nabla} \cdot \boldsymbol{u} = 0, \tag{2.1}$$

https://doi.org/10.1017/jfm.2019.666 Published online by Cambridge University Press

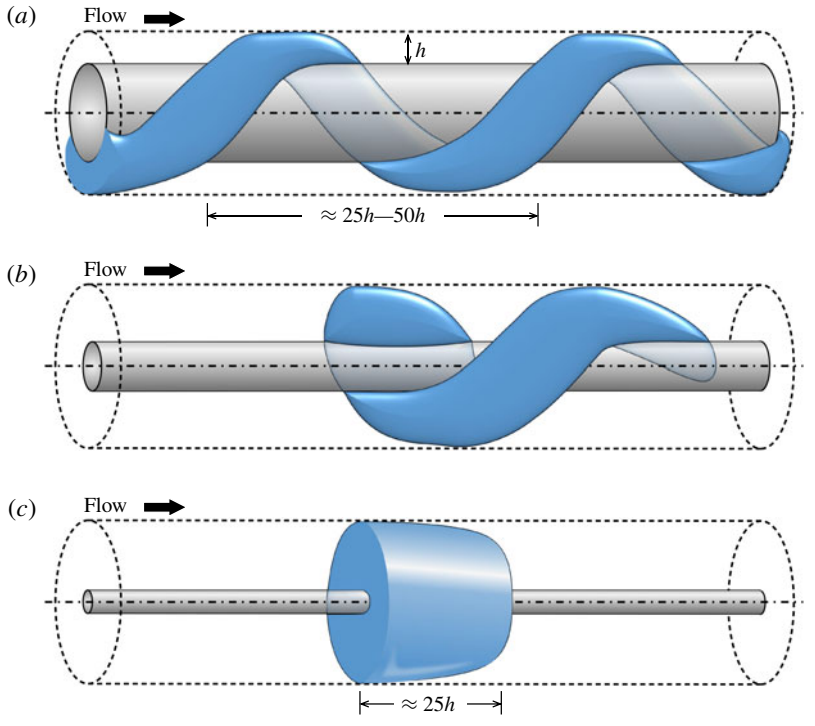


FIGURE 3. (Colour online) Typical transitional structures in annular flow geometries depending on η, according to Ishida *et al.* (2016). Blue regions represent localised turbulence. The aspect ratio (gap versus streamwise length) is changed for each panel. (*a*) Helical turbulence for high η, (*b*) helical puff for intermediate η and (*c*) straight puff for low η.

$$\frac{\partial \boldsymbol{u}}{\partial t} + (\boldsymbol{u}\cdot\boldsymbol{\nabla})\boldsymbol{u} = -\boldsymbol{\nabla} p + \frac{1}{Re}\nabla^2\boldsymbol{u}, \tag{2.2}$$

where p is the reduced pressure field. The fluid density is unity.

The Reynolds number is defined as $Re \equiv u_w h/4\nu$, with ν the kinematic viscosity of the fluid. The total wall shear stress is linked to the friction Reynolds number Re_τ, defined as

$$Re_\tau = \frac{u_\tau h}{2\nu}. \tag{2.3}$$

It is based on the friction velocity u_τ evaluated at each wall using the formula

$$u_\tau = \frac{\eta u_{\tau,inner} + u_{\tau,outer}}{\eta + 1}, \tag{2.4}$$

where each u_τ is defined by the corresponding wall shear stress τ_w and by the relation $\tau_w = \rho u_\tau^2$, from which inner units can be defined (see table 1).

The boundary conditions are periodicity in the streamwise (x) and the azimuthal coordinates (θ), and no slip at the walls:

$$\boldsymbol{u} = (1, 0, 0) \quad \text{at } r = r_i \text{ (or } y = 0), \tag{2.5}$$

https://doi.org/10.1017/jfm.2019.666 Published online by Cambridge University Press

η	0.1	0.5	0.8
Re	$750 \to 390$	$750 \to 377.5$	$750 \to 325$
Re_τ	$34.5 \to 14.7$	$49.0 \to 18.8$	$51.3 \to 18.1$
$R_i,\ R_o$	$0.111h,\ 1.11h$	$h,\ 2h$	$4h,\ 5h$
$L_x \times L_r \times L_\theta$	$204.8h \times h \times 2\pi$	$102.4h \times h \times 2\pi$	$102.4h \times h \times 2\pi$
$L_{zi},\ L_{zo}$	$0.698h,\ 6.98h$	$6.28h,\ 12.6h$	$25.1h,\ 31.4h$
$N_x \times N_r \times N_\theta$	$1024 \times 64 \times 256$	$1024 \times 64 \times 256$	$1024 \times 64 \times 512$
Δx	$0.2h$	$0.1h$	$0.1h$
Δr	$0.00132h$–$0.0316h$	$0.00132h$–$0.0316h$	$0.00132h$–$0.0316h$
$\Delta z_i,\ \Delta z_o$	$0.00273h,\ 0.0273h$	$0.0245h,\ 0.0491h$	$0.0491h,\ 0.0614h$
Δx^+	2.94–6.90	1.88–4.92	1.81–5.13
Δr^+	0.0387–1.09	0.0495–1.56	0.0477–1.62
Δz^+	0.0400–0.940	0.461–2.42	0.888–3.15

TABLE 1. Computational conditions for aCf with nominal azimuthal extent $L_\theta = 2\pi$: radius ratio η, Reynolds number Re, friction Reynolds number Re_τ, inner radius R_i, outer radius R_o, computational domain dimensions $L_x \times L_r \times L_\theta$, inner perimeter L_{zi}, outer perimeter L_{zo}, number of grid points $N_x \times N_r \times N_\theta$, and range of values for the increments Δj ($j = x, r, \theta$ (or z)). The superscript ($^+$) denotes the normalisation by wall units based on u_τ and ν.

$$\boldsymbol{u} = (0, 0, 0) \quad \text{at } r = r_o \ (\text{or } y = 1), \tag{2.6}$$

$$\boldsymbol{u}(0, r, \theta) = \boldsymbol{u}(L_x, r, \theta), \tag{2.7}$$

$$\boldsymbol{u}(x, r, 0) = \boldsymbol{u}(x, r, 2n\pi). \tag{2.8}$$

In the last boundary condition (2.8) expressing the azimuthal periodicity, the value of n is usually $n = 1$. Choosing n as a fraction of the form $1/m$, with m a positive integer, would correspond to imposing an additional discrete azimuthal symmetry. In § 3, we will take the original choice of considering n as a positive integer such as $n = 1, 2, 3, \ldots$. Such a boundary condition leads to an azimuthal coordinate ranging from 0 to $2\pi n$, which for $n > 1$ lacks direct physical interpretation. This is intended here as a numerical trick in order to question the effect of confinement by the boundary conditions.

The governing equations (2.1)–(2.2) together with the boundary conditions (2.5)–(2.8) admit a steady axial solution of the form

$$U_{base}(y) = \frac{\ln\left[y(1-\eta)+\eta\right]}{\ln \eta}, \tag{2.9}$$

interpreted as the laminar base flow. For $\eta \to 1$, U_{base} converges in a non-singular way towards the linear profile $U_{base}(y)|_{\eta=1} \sim (1-y)$ which is consistent with the pCf limit. Figure 2 displays profiles of $U_{base}(y)$ parameterised by η ranging down to 10^{-5}, for which the profile unambiguously differs from that in cylindrical pipe flow.

2.2. *Numerical tools*

Equation (2.2) is discretised in space using finite differences. The time discretisation is carried out using a second-order Crank–Nicolson scheme and an Adams–Bashforth scheme for the wall-normal viscous term and the other terms, respectively. Further details about the numerical methods used here can be found in Abe, Kawamura & Matsuo (2001).

https://doi.org/10.1017/jfm.2019.666 Published online by Cambridge University Press

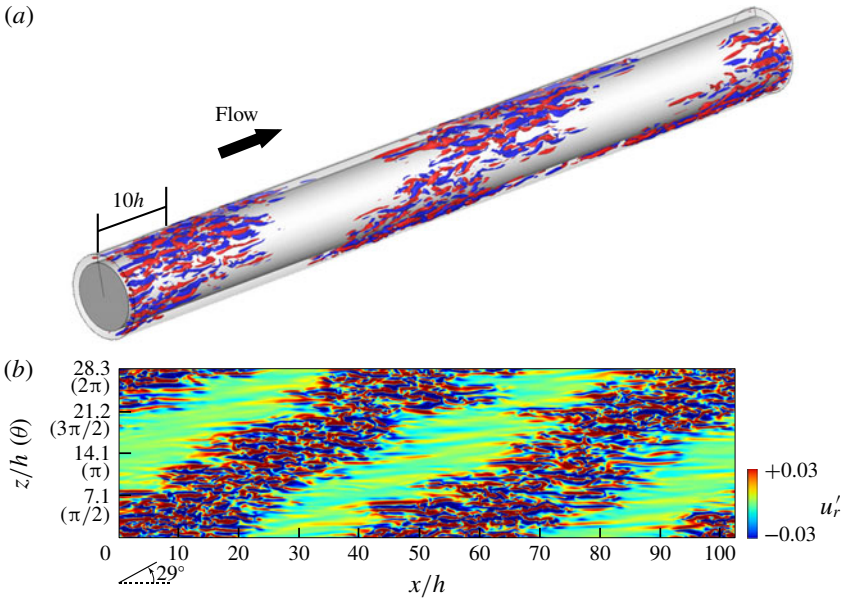


FIGURE 4. (Colour online) Instantaneous flow field of aCf for $\eta = 0.8$ and $Re = 350$, accompanied by helical turbulence. (*a*) Three-dimensional visualisation by iso-surfaces of wall-normal velocity fluctuations ($u_r' = -0.03$, blue; $u_r' = 0.03$, red); (*b*) two-dimensional contour of u_r' in the x–z (or x–θ) plane at mid-gap. The pattern propagates steadily towards $x > 0$ (to the right in the figure).

The tested radius ratios are 0.8, 0.5 and 0.1, and the other numerical parameters are shown in table 1. The number of grid points in the azimuthal direction is 256 for $\eta = 0.1$ and 0.5 with the non-uniform radial mesh, but we used 512 grid points for $\eta = 0.8$ because of its wider domain relative to the gap h. The strategy to isolate the transitional regimes of aCf is similar to that used in aPf. First, using an arbitrary finite-amplitude initial condition, a turbulent flow is computed at large enough Re for which no laminar–turbulent coexistence is expected. In a second phase, Re is decreased in small steps until the flow can be considered statistically steady based on energy time series. Visual inspection of the flow fields at mid-gap is used to decide whether or not the flow displays laminar–turbulent coexistence.

3. Morphology of coherent structures

3.1. *High* $\eta = 0.8$

We begin the exploration of the intermittent regimes by considering a relatively high value of $\eta = 0.8$, for which the curvature is weak and aCf is expected to behave like pCf. Figure 4 shows the wall-normal velocity of a typical flow field for $\eta = 0.8$ and $Re = 350$. The unfolded plane of two-dimensional contours in figure 4(*b*) lies at mid-gap ($y = 0.5$) where the corresponding spanwise width is $28.3h$. Measurements of the friction Reynolds number yield $Re_\tau = 25.2$. Expressed in wall units, the domain size visualised in figure 4(*b*) is equivalent to $L_x^+ \times L_z^+ = 5160 \times 1430$. As expected, the large-scale spatial patterning of the flow field is evident whereas at smaller scales streamwise streaks dominate. The turbulent region wraps around the inner cylinder in the form of a helix, whose pitch angle is approximately 29° with respect to the x axis.

https://doi.org/10.1017/jfm.2019.666 Published online by Cambridge University Press

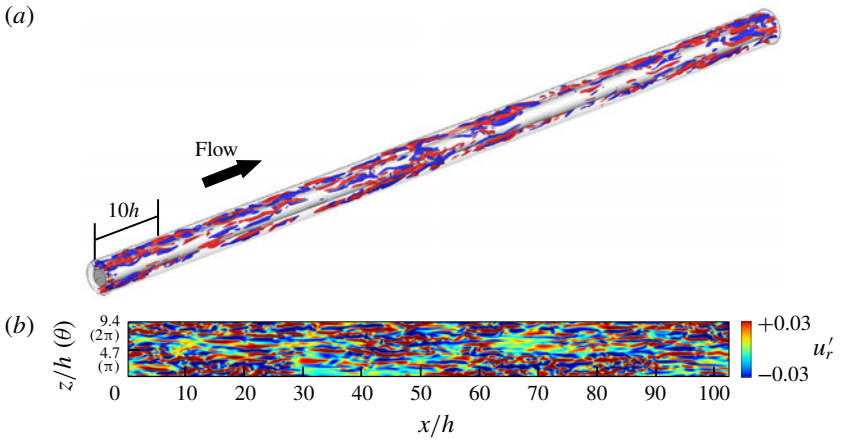


FIGURE 5. (Colour online) Same as figure 4 for $\eta = 0.5$ and $Re = 387.5$, featuring laminar patches.

The laminar streamwise intervals have lengths of about $50h$, consistent with those in pCf (Prigent *et al.* 2002; Duguet *et al.* 2010*a*; Brethouwer *et al.* 2012). Such helical turbulence also occurs in aPf (Ishida *et al.* 2016) with a similar value of the pitch angle. By reducing Re, the helical turbulence sustains until $Re = 337.5$ ($Re_\tau = 24.0$) and eventually decays at 325. This scenario and the estimated value for Re_g are fully consistent with those for pCf, despite the curvature of the walls.

3.2. *Moderate* $\eta = 0.5$

3.2.1. *Nominal parameters*

Let us now focus on the moderate-η regime by analysing the case $\eta = 0.5$. Note that in the context of aPf, the transitional regime for $\eta = 0.5$ differs little from the case $\eta = 0.8$. The analysis in Ishida *et al.* (2017) shows that for $\eta > \eta_c \approx 0.3$, the perimeter is sufficiently large (in units of h) for large-scale flows to form, and as a consequence localised turbulence can only take the shape of helical puffs as in figure 3(*b*) or helical stripes for even higher η. At these marginal Reynolds numbers, the smallest vortical structures occupy the whole gap and h is hence the convenient reference length scale. The fact that h defines the order of magnitude for the size of the smallest length scales has been suggested as the condition defining marginality (Alfredsson & Matsubara 2000).

Whereas helical stripes prevail for $\eta = 0.8$, they are absent from the simulations at $\eta = 0.5$. A typical flow regime obtained for $Re = 387.5$ is displayed in figure 5. In this case, the azimuthal length is only $9.4h$ at mid-gap, which is shorter than the (intrinsic) laminar interval of turbulent bands. As a result, despite a furtive occurrence, proper helical turbulent bands cannot sustain as organised structures. Some disorganised laminar patches can be observed in practice near $Re = 380$ ($Re_\tau = 27.2$). Decreasing Re further, the turbulent regions become intermittent in the streamwise direction but no band-like or puff-like structure forms. The flow eventually relaminarises at $Re = 377.5$, a value unambiguously higher than the threshold value for $\eta = 0.8$.

3.2.2. *Azimuthally extended system*

As mentioned in the introduction, two intermingled factors can influence the formation of large-scale structures in comparison with the planar case: the azimuthal

https://doi.org/10.1017/jfm.2019.666 Published online by Cambridge University Press

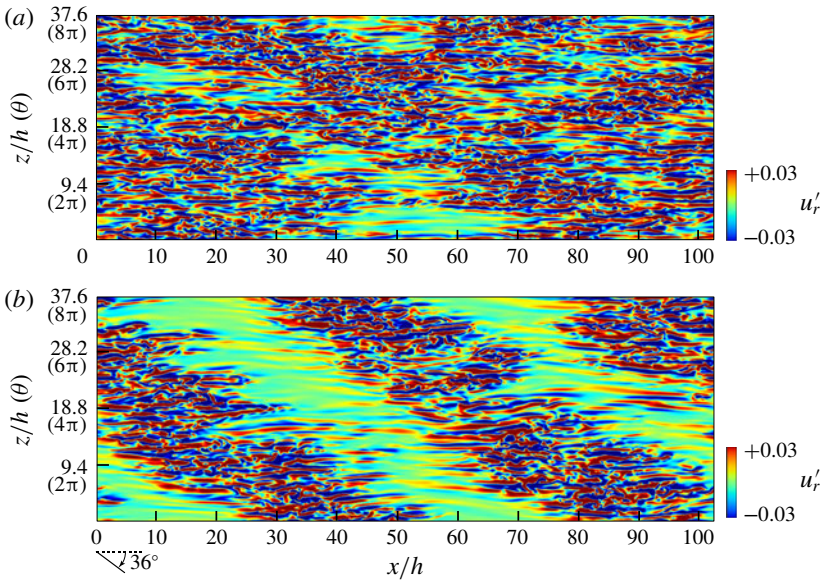


FIGURE 6. (Colour online) Simulations with artificial azimuthal extension $L_\theta = 8\pi$. Contours show instantaneous wall-normal velocity fluctuations u_r' in the x–z (or x–θ) plane at mid-gap for $\eta = 0.5$. These flows are in a statistically steady state. (*a*) Reynolds number $Re = 387.5$, irregular laminar patches; (*b*) $Re = 350$, helical turbulence.

extent and the wall curvature. We use a numerical trick to test whether the obtained flows persist in the absence of azimuthal confinement without modifying the wall curvature, namely by simulating the flow in a domain where the azimuthal variable describes the range $(0, 2n\pi)$ with $n > 1$. The hypothesis $L_\theta > 2\pi$ should be seen as a deliberate validation technique rather than as the introduction of an esoteric parameter.

The strategy to seek transitional regimes featuring laminar subdomains is similar to that for $L_\theta = 2\pi$. For the case $\eta = 0.5$, we have tried several integer values of n until visual inspection of the flow fields reveals some clear changes with respect to $n = 1$. The case $n = 4$ corresponds to a periphery of $L_\theta = 8\pi$, i.e. four nominal peripheries, and the perimeter values at the inner wall, at mid-gap and at the outer wall are $(L_{zi}, L_{zc}, L_{zo}) = (25.1h, 37.6h, 50.2h)$, respectively. The number of azimuthal grid points is increased to $N_\theta = 512$, hence doubled in resolution with respect to $n = 1$. In other words there was a trade-off in the numerical resolution, resulting probably in a quantitative shift of the Reynolds numbers. The extended azimuthal grid spacings on the outer and inner walls are, respectively, $\Delta z = 0.098h$ and $0.049h$, which remain adequate resolutions when expressed in inner units since they verify $\Delta z^+ \leqslant 5$.

Figure 6 shows two-dimensional distributions of the wall-normal velocity in the x–z (or x–θ) plane at mid-gap. At $Re = 387.5$, laminar patches can be found, and there are no strong differences between the cases $L_\theta = 2\pi$ (figure 5*b*) and $L_\theta = 8\pi$ (figure 6*a*). By reducing Re further down to 350, helical turbulence occurred for $L_\theta = 8\pi$ (figure 6*b*), whereas the flow was fully laminar at the same value of Re for $L_\theta = 2\pi$. The pitch angle α_θ is 36° with respect to the streamwise direction, which appears comparable to the value of 29° reported for $\eta = 0.8$. Such a slight difference is trivial in the present study, because α_θ is dictated by the domain aspect ratio

https://doi.org/10.1017/jfm.2019.666 Published online by Cambridge University Press

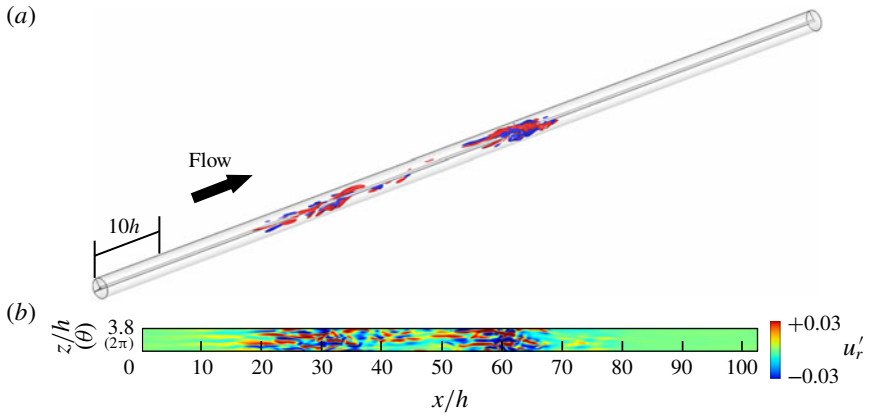


FIGURE 7. (Colour online) Same as figure 4, but for $\eta = 0.1$ and $Re = 400$, featuring puff-like structures. Only half the axial length of the computational domain is displayed.

via the geometric relation $\alpha_\theta = \tan^{-1}(pL_z/mL_x)$, with p and m integers. This helical turbulence regime is found to relaminarise at $Re = 325$, which is similar to the case $\eta = 0.8$ and to pCf.

As a temporary conclusion, unlike aPf, the flow in realistic aCf does not feature any helical puff or stripe for $\eta = 0.5$. Nevertheless, artificial azimuthal extension of the numerical domain, without change of curvature, reveals that helical stripes can in fact be sustained if the perimeter reaches 8π. This suggests that the lack of occurrence of helical large-scale structures in aCf with $\eta = 0.5$ is not due to the wall curvature, but to geometric confinement.

3.3. *Low* $\eta = 0.1$

3.3.1. *Nominal parameters*

For $\eta = 0.1$, no oblique laminar–turbulent interface was observed in our simulations, neither as a permanent regime nor even transiently. By direct analogy with aPf, for which no helical structure was ever detected below $\eta \leqslant 0.3$, the immediate conclusion is that $\eta = 0.1$ is too low for banded turbulence to occur. There are, however, clear signs of laminar–turbulent coexistence: coherent structures localised in the streamwise direction only, similar to puffs in pipe flow, have been visualised for Re strictly below 400. These structures are referred to as 'puff-like' because there are both common points and dissimilarities with the puffs found in pipe flow intermittency. Several such puff-like structures are shown in figure 7 to coexist for $Re = 400$. Their long-time dynamics suggests that they are in equilibrium; however, if these coherent structures decay after a sufficiently longer time, the flow goes back to the globally laminar state and puffs are only metastable objects. At slightly higher Re, splitting of some of the puffs is also observed. All these features have been reported as robust statistical properties of cylindrical pipe flow (Shimizu *et al.* 2014).

Figure 8 illustrates the spatiotemporal intermittency found for $\eta = 0.1$. Two space–time diagrams for $Re = 400$ and 395 show the azimuthally averaged streamwise velocity $\langle u_x \rangle_\theta = \int u_x \mathrm{d}\theta/2\pi$, evaluated at mid-gap as a function of x and t. In both cases, perturbations appear close to the laminar–turbulent interface. They can propagate in both upstream and downstream directions from the core of the puff towards the laminar flow. This makes the puff appear more symmetric than its pipe

https://doi.org/10.1017/jfm.2019.666 Published online by Cambridge University Press

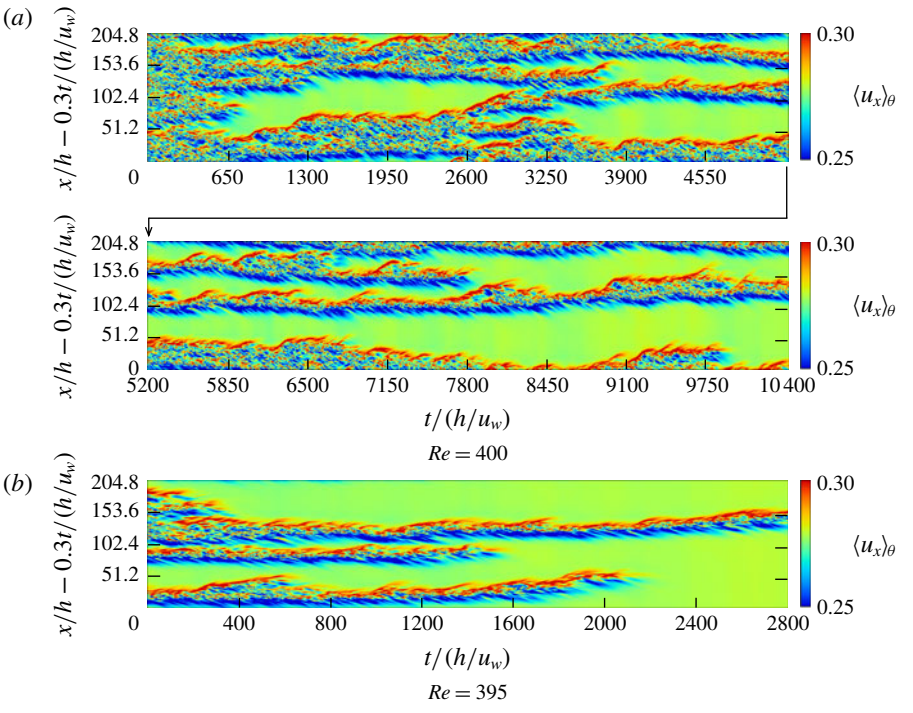


FIGURE 8. (Colour online) Spatiotemporal diagrams of the azimuthally averaged streamwise velocity $\langle u_x \rangle_\theta$ at mid-gap for $\eta = 0.1$ and $L_\theta = 2\pi$: (*a*) $Re = 400$; (*b*) $Re = 395$. The vertical axis shows the streamwise distance in a frame of reference moving at streamwise speed $0.3u_w$.

flow counterpart, where most perturbations are advected towards decreasing pressure (Shimizu *et al.* 2014). For the case $Re = 400$ (figure 8*a*), the flow apparently settles to a statistically steady state for $t \geqslant 5000h/u_w$. One can identify locally transient quasi-laminar regions, but no clear wavelength or patterning emerges. It should be pointed out that no quasi-one-dimensional shear flow has ever shown convincing patterning properties with well-defined wavelengths.

For $Re = 395$ (figure 8*b*), all turbulent puff-like structures are found to decay. According to the measurements above, the critical point for $\eta = 0.1$ lies between $Re = 400$ and 395. If normalised by the hydraulic diameter ($2h$) and the 'centreline velocity' u_w as in pipe flow, this critical point corresponds to $4Re = 1590 \pm 10$ lower than the value of 2040 ± 10 for cylindrical pipe flow (Avila *et al.* 2011).

3.3.2. *Azimuthally extended system*

As before, we wish to go beyond the mere observation that no oblique pattern forms for $\eta = 0.1$ and explain which mechanism, confinement or curvature, is responsible for the different structure of the turbulent flow at its onset. We hence report direct numerical simulations for $\eta = 0.1$ in an azimuthally extended numerical domain with $L_\theta = 16\pi$ ($n = 8$ times longer than the nominal circumference). In this case, $(L_{zi}, L_{zc}, L_{zo}) = (5.58h, 30.4h, 55.8h)$ and the resolution is kept to $N_\theta = 512$ with $\Delta z^+ \leqslant 3$. We note that the concept of 'extended system' depends here highly on the radial position. This is an unavoidable geometric consequence of the relative

https://doi.org/10.1017/jfm.2019.666 Published online by Cambridge University Press

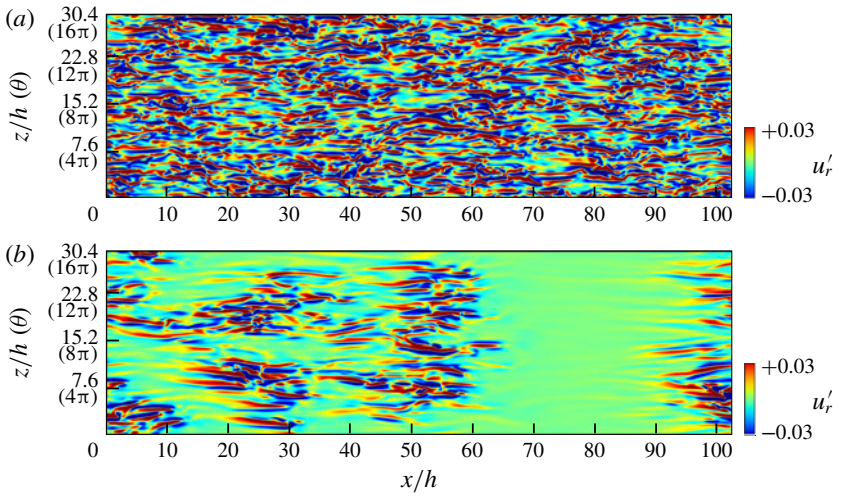


FIGURE 9. (Colour online) Instantaneous visualisation of wall-normal velocity fluctuations u_r' at mid-gap for $\eta = 0.1$ and $L_\theta = 16\pi$, and at (*a*) $Re = 400$ and (*b*) $Re = 275$. The supplementary movie shows the time evolution during an arbitrary $800h/u_w$ of the flow visualised in (*b*), demonstrating a new regime of dynamic laminar–turbulent coexistence.

smallness of the inner rod. One effect of the azimuthal extension is again a marked shift of Re_g: the flow does not return to laminar even at $Re = 275$, a value much lower than Re_g for $L_\theta = 2\pi$. Since the numerical resolution is still satisfactory according to table 1, the shift in Re_g is not attributed to the coarser resolution but to the change in boundary conditions. The nominal aCf with $\eta = 0.1$ relaminarises at $Re \approx 400$, this onset Reynolds number being strongly lowered for larger $L_\theta = 16\pi$ (figure 9*a*) since relaminarisation in finite time has been observed for all $Re \leqslant 262.5$. For the values of Re where turbulence was detected, transiently or sustained, the flow displays laminar–turbulent coexistence, but never displays any helically shaped turbulence, as can be seen in figure 9(*b*) (see also the supplementary movie available at https://doi.org/10.1017/jfm.2019.666, which highlights the dynamical behaviour of the new flow regime). Note that the average streak width remains unaffected by the azimuthal extension beyond 2π. Given the very large perimeter of the outer wall in units of h, large enough in principle to accommodate one wavelength of a turbulent band, the absence of helical band, or equivalently of azimuthal large-scale flow, cannot be assigned to the azimuthal confinement, even though the inner perimeter is itself too small to accommodate this wavelength. We thus deduce that, unlike for $\eta = 0.5$, the wall curvature is responsible for the inability of the geometry to sustain helical stripe patterns for $\eta = 0.1$.

Figure 10 shows visualisations of the same turbulent flow for $\eta = 0.1$ at three different radii. It confirms that the topology of the flow is only weakly dependent on the radial value. Although azimuthal circumferences (L_z/h) differ between the three panels, the observed irregular patterns of localised turbulence are very similar to each other and match well when plotted versus θ. As also confirmed in the supplementary movie, small-scale structures in turbulent patches seem to penetrate the entire gap from the inner to the outer wall. The intensity of velocity fluctuations in the region near the outer wall is weaker than near the inner wall, as also shown in figure 10 (using different colourbars). The figure also makes the absence of large-scale helical

https://doi.org/10.1017/jfm.2019.666 Published online by Cambridge University Press

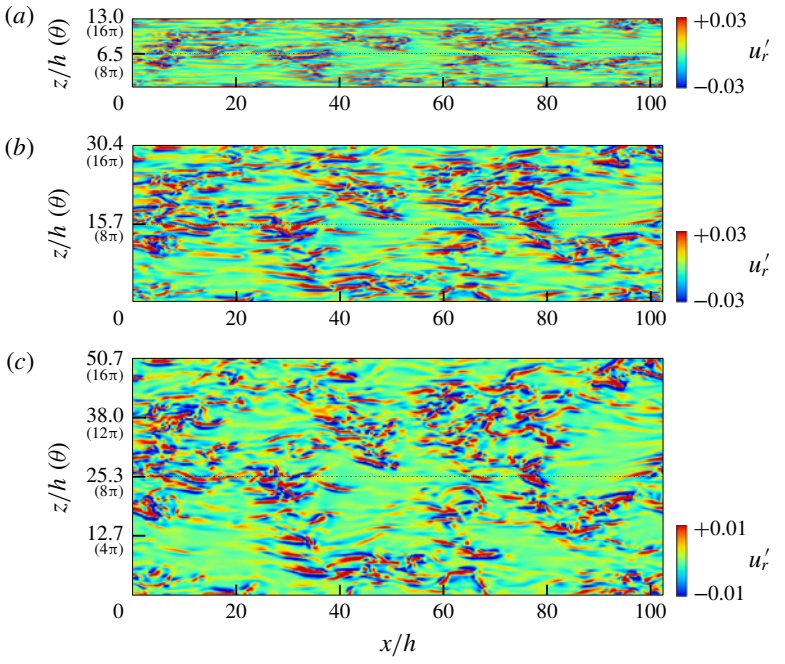


FIGURE 10. (Colour online) Instantaneous visualisation of wall-normal velocity fluctuations u_r' in x–θ planes at three different radial positions for $\eta = 0.1$, $L_\theta = 16\pi$ and $Re = 300$. From top to bottom: (*a*) $y \approx 0.15$ (near the inner wall), (*b*) $y \approx 0.5$ (mid-gap) and (*c*) $y \approx 0.9$ (near the outer wall).

pattern clear at any radial position. There is always a possibility that for sufficiently large azimuthal extension, both inner and outer perimeters become large enough to accommodate long-wavelength turbulent patterns again, yet with a very small pitch angle that cannot be captured for smaller L_θ. However, given the present low value of η, this would imply even longer computational domains and hence very expensive simulation. This hypothesis is hence not considered in what follows.

Among the many implications of wall curvature, an interesting one which can be checked for in simulations, in analogy with the corresponding laminar profiles, is the statistical asymmetry of the turbulent flow with respect to the mid-gap (this symmetry is exact only in the limit $\eta \to 1$). Figure 11 shows the azimuthal vorticity and streamwise velocity inside an arbitrary meridian x–r plane. The moving inner rod is located at the top of the figure while the outer rod lies at its bottom. Strong mean gradients of azimuthal vorticity (the 'boundary layer') are found near the inner wall only. This boundary layer triggers ejections of vorticity towards the outer wall, at various places corresponding to the location of the turbulent patch. This calls for a comparison with the regeneration mechanisms discussed in the context of pipe flow puffs (Shimizu & Kida 2009; Duguet, Willis & Kerswell 2010*b*; Hof *et al.* 2010), where transverse vorticity acts as a source of perturbations that re-energises the turbulent puff against its own viscous decay. In these studies, the perturbations triggered by the instability of the corresponding shear layer are advected downstream, out of the puff. In the present context of aCf for $\eta = 0.1$, the perturbations emanating from the shear layer at the inner rod are advected upstream in the frame moving with the inner wall. This suggests a turbulence regeneration process of a different kind.

https://doi.org/10.1017/jfm.2019.666 Published online by Cambridge University Press

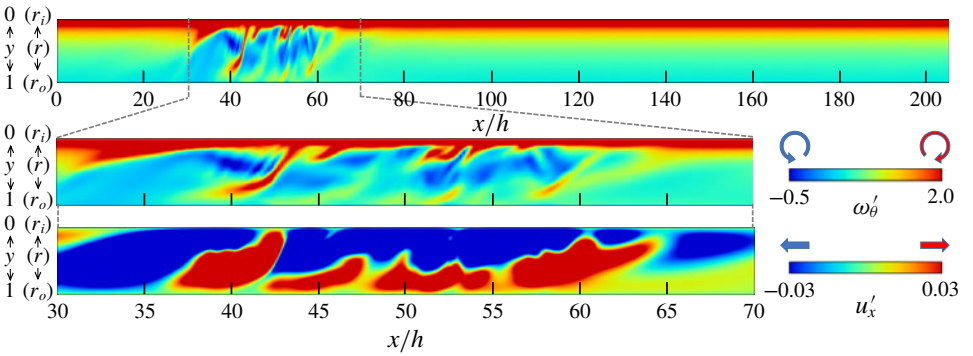


FIGURE 11. (Colour online) Typical snapshots of azimuthal vorticity ω'_θ (two top rows) and streamwise velocity fluctuation u'_x (bottom row) distributions in an x–r plane of aCf for $\eta = 0.1$ and $Re = 395$ with nominal $L_\theta = 2\pi$. The inner rod (top boundary) moves towards the right of the figure.

More work is needed to relate rigorously this observation to the short coherence length of these patches, as will be discussed in the next section. Section 4 is devoted to a deeper quantitative analysis of the statistical properties of all the laminar–turbulent coexistence regimes identified in this section.

4. Statistics

The statistics presented in this section have been gathered from the numerical runs described in the previous section. The cases simulated with $L_\theta = 2\pi$ are summed up in table 1, while the two azimuthally extended simulations, $\eta = 0.5$ with $L_\theta = 8\pi$ and $\eta = 0.1$ with $L_\theta = 16\pi$, are described in §§ 3.2.2 and 3.3.2, respectively. Importantly, all spatial statistics presented here are averaged over the whole spatial domain (or sometimes over the mid-gap only), but are not conditional: these are not statistics over the turbulent zones only, rather global statistics of laminar–turbulent coexistence seen as a single regime.

4.1. *Mean velocity profile*

The mean streamwise velocity profiles are displayed in figure 12. Here, the vertical axis y $(= r - r_i)$ is the radial distance to the wall measured from the inner cylinder. The overbar denotes time-averaging in space over the two variables x and z, and in time over a time horizon T. Let Re_g be the lowest value of Re where turbulence is found for each value η, and let us assume by convention that it indicates relaminarisation for $Re < Re_g$, while in the other cases turbulence could sustain at least until time T, with T limited here to $O(10^4)$. Our results indicate that Re_g has a strong dependence on η. Mean velocity profiles, evaluated here only for Re close to $Re_g(\eta)$, are also affected by η. The dashed-dotted lines indicate the laminar profiles, in agreement with the theoretical solutions given in (2.9) as well as in figure 2. We note that for $\eta = 0.1$ for instance, the profile for $Re = 390$ deviates from the cluster formed by the other profiles reported for $400 \leqslant Re \leqslant 750$. The last observation results from the inclusion *de facto* of the laminar parts in the spatial averaging: any variation in the mean turbulent fraction (which will be documented in §4.4) has an impact on the mean velocity profile.

https://doi.org/10.1017/jfm.2019.666 Published online by Cambridge University Press

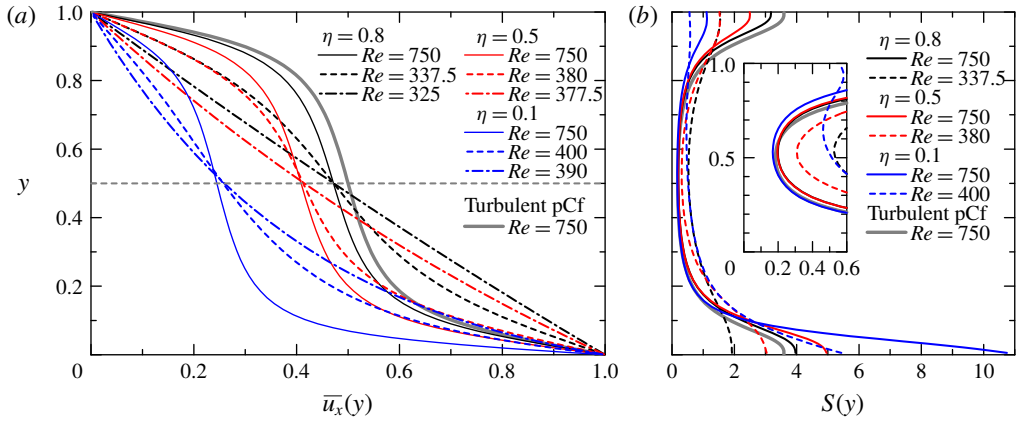


FIGURE 12. (Colour online) Mean profiles of the streamwise velocity (*a*) and its velocity gradient S (*b*) for various η and Re. Black, red and blue lines show $\eta = 0.8$, 0.5 and 0.1, respectively. The dashed-dotted lines are of laminar profiles and in agreement with the theoretical solution. For reference, a velocity profile of turbulent pCf (Tsukahara, Kawamura & Shingai 2006) is also shown.

A clear trend emerges from all the non-laminar cases reported in figure 12: the mean velocity profiles are S-shaped and all display an inflection point located near $y = 0.5$. The symmetric property, which the limiting case of pCf also possesses, apparently persists in all aCf configurations despite the broken symmetry of the system with respect to the mid-gap. This does not necessarily imply shear instabilities yet. Recalling the novel kind of laminar–turbulent coexistence identified for low $\eta = 0.1$, it is interesting to compare how the mean profile evolves with decreasing η. Other features of interest can be extracted from figure 12(*b*), such as the mean shear profile, given by $S(y) := -\partial\overline{u_x}/\partial y$. As η decreases, this velocity gradient becomes steeper at the inner cylinder than at the outer one. The profile also becomes more and more asymmetric with respect to the mid-gap $y = 0.5$. A quantitative comparison is given for $Re = 750$, a case for which statistics are not affected by laminar–turbulent coexistence. While $S(y)$ is approximately 0.2 at mid-gap for all values of η, its value ranges from 1 to 3 at the outer wall (decreasing with decreasing η) and from 4 to 11 at the inner wall (now increasing with decreasing η). The trend is hence such that, as η decreases towards 0.1, the mean profile gets more asymmetric, and resembles more and more a simple linear boundary layer profile located near the inner rod, while the gradients at the outer rod are increasingly weak.

4.2. *Friction factor*

We present here calculations of the friction coefficient C_f versus Re, displayed in figure 13. To the authors' knowledge, no experimental study has examined C_f of aCf except for Shands, Alfredsson & Lindgren (1980), who reported measurements in a wide range of Reynolds number including laminar and fully developed turbulent regimes for low $\eta < 0.03$. The coefficient C_f for the present study is defined as

$$C_f = \frac{2\tau_w}{(\xi u_w)^2}, \tag{4.1}$$

https://doi.org/10.1017/jfm.2019.666 Published online by Cambridge University Press

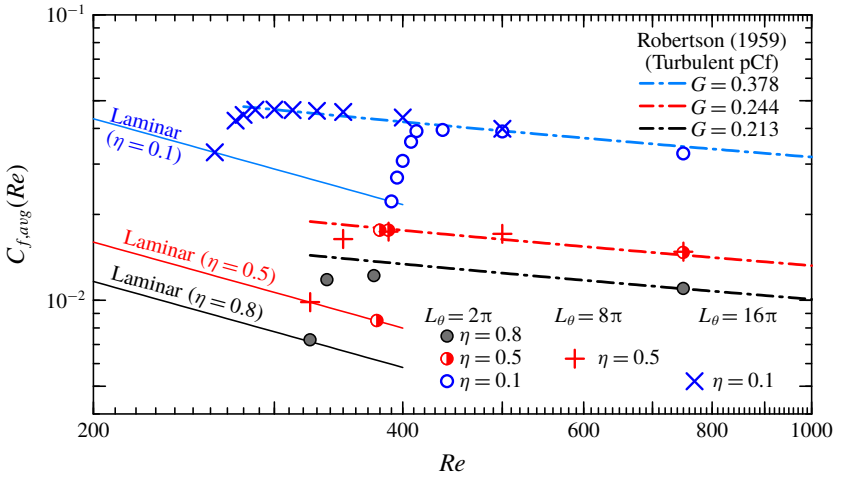


FIGURE 13. (Colour online) Friction coefficient as a function of Re including the cases of artificially extended L_θ. Solid and dashed-dotted lines show (4.3) and (4.4), respectively.

where the coefficient ξ stands for the ratio between the dimensional bulk velocity and the dimensional wall velocity u_w. Note that τ_w and ξ are both defined as temporal averages. The introduction of the ratio ξ is intended to capture the dependence of the bulk-mean velocity on η. For instance, ξ should be 0.5 for the case $\eta = 1$. In this series of numerical experiments, we obtained $\xi = 0.46$ ($\eta = 0.8$), $\xi = 0.39$ ($\eta = 0.5$) and $\xi = 0.20$ ($\eta = 0.1$). In figure 13, the plotted quantity $C_{f,avg}$ is a weighted average between the inner and outer values of C_f, i.e.

$$C_{f,avg} = \frac{\eta C_{f,inner} + C_{f,outer}}{\eta + 1}, \tag{4.2}$$

where each C_f is computed from the wall shear stress τ_w measured locally. The solid line shows the laminar law given by

$$C_{f,laminar} = \frac{4}{\xi^2} \frac{1 - \eta}{Re(1 + \eta)|\ln \eta|}, \tag{4.3}$$

and the dashed-dotted line is the empirical law suggested by Robertson (1959) for turbulent pCf:

$$\sqrt{\frac{C_f}{2}} = \frac{G}{\log Re}. \tag{4.4}$$

Circles and crosses label the results with nominal and extended L_θ, respectively. The constant G is determined by a logarithmic fit of $\sqrt{C_f}$ directly from the simulations.

We start by describing the results obtained for standard numerical domains with $L_\theta = 2\pi$. We first note that Robertson's formula, borrowed from the plane Couette case, captures surprisingly well the turbulent regime for all values of η as long as Re is large enough (above 500). A 'transitional' region, i.e. a range comprising both non-laminar and non-fully turbulent regions, emerges for $325 < Re < 400$ (for $\eta = 0.8$)

https://doi.org/10.1017/jfm.2019.666 Published online by Cambridge University Press

and $395 < Re < 412$ (for $\eta = 0.1$). As for $\eta = 0.5$, the turbulent flow becomes laminar at $Re = 377.5$ and, hence, no intermediate value of C_f between laminar and turbulent values was identified. From figure 13, Re_g can be approximated by 325, 380 and 400 for $\eta = 0.8$, 0.5 and 0.1, respectively.

In the cases of artificially extended L_θ (crosses in figure 13), the variations of C_f exhibit different but still interesting trends. For $\eta = 0.5$, Re_g of $L_\theta = 8\pi$ (red crosses) is lower than that of $L_\theta = 2\pi$ and the new value of $Re_g = 325$ is similar to the threshold Reynolds number reported in pCf by Duguet *et al.* (2010*a*). For $\eta = 0.1$, the lower value of Re_g has already been reported in the previous section. It is surprising that C_f is very close to the fully turbulent value (see the blue crosses), even at $Re = 300$, although the flow field is much more intermittent than at higher Re (as will be quantified by the turbulent fraction in § 4.4).

4.3. *Two-point correlations*

After describing statistics involving streamwise and azimuthal averages, we now describe the spatial correlations in the case of laminar–turbulent coexistence (i.e. close to Re_g), restrained to the wall-parallel variables x and θ. The correlations of the velocity perturbations, evaluated at a constant value of $y = y_{ref}$, are classically defined, after normalisation, by

$$R_{ii}(\Delta x) = \frac{\overline{u_i'(x, y_{ref}, \theta) \cdot u_i'(x + \Delta x, y_{ref}, \theta)}}{\overline{u_i'(x, y_{ref}, \theta)^2}}, \tag{4.5}$$

$$R_{ii}(\Delta \theta) = \frac{\overline{u_i'(x, y_{ref}, \theta) \cdot u_i'(x, y_{ref}, \theta + \Delta\theta)}}{\overline{u_i'(x, y_{ref}, \theta)^2}}, \tag{4.6}$$

where the overbar $\overline{(\cdot)}$ again denotes averaging over x, θ and time. The value of y_{ref} is approximately 0.5, i.e. close to mid-gap. The present focus is on a neater characterisation of the new regime identified for $\eta = 0.1$ in the extended domain with $L_\theta = 16\pi$. To this end, we compare in figure 14 the autocorrelations of each velocity component as functions of the streamwise and azimuthal spatial lags Δx and $\Delta\theta$, computed for $\eta = 0.1$, to their counterparts for $L_\theta = 2\pi$, as well as to the other extended case with $\eta = 0.5$ and $L_\theta = 8\pi$. The results obtained for $L_\theta = 2\pi$ are not significantly different between $\eta = 0.5$ and 0.1 (not shown here), because of the common absence of large-scale patterning apparent in figure 5.

These correlations fall into two groups with well-defined trends in each group. The first trend (figure 14*a–e*) includes the autocorrelations of streamwise and radial velocity components for both streamwise and azimuthal lags: streamwise correlation curves differ weakly from case to case, but the axial correlation length is less than $5h$. This appears significantly shorter than the minimum puff spacing away from criticality, i.e. 20–30 diameters or larger values for lower Reynolds numbers (Samanta, de Lozar & Hof 2011). The case with $\eta = 0.5$ displays a comparable streamwise correlation length for the streamwise and radial velocity components, but shorter azimuthal correlations, while for $\eta = 0.1$ both values of L_θ yield similar lag angles of approximately π.

The second trend (figure 14*c*,*f*) is for the correlations of the azimuthal velocity field: the correlation lengths in x and θ for $\eta = 0.5$ are very large, respectively $26h$ and 2π, because of the large-scale structure of the turbulent bands. For $\eta = 0.1$, however, they shrink to respectively $\approx 5h$ and less than $\pi/2$. For comparison with the case $\eta = 0.1$,

https://doi.org/10.1017/jfm.2019.666 Published online by Cambridge University Press

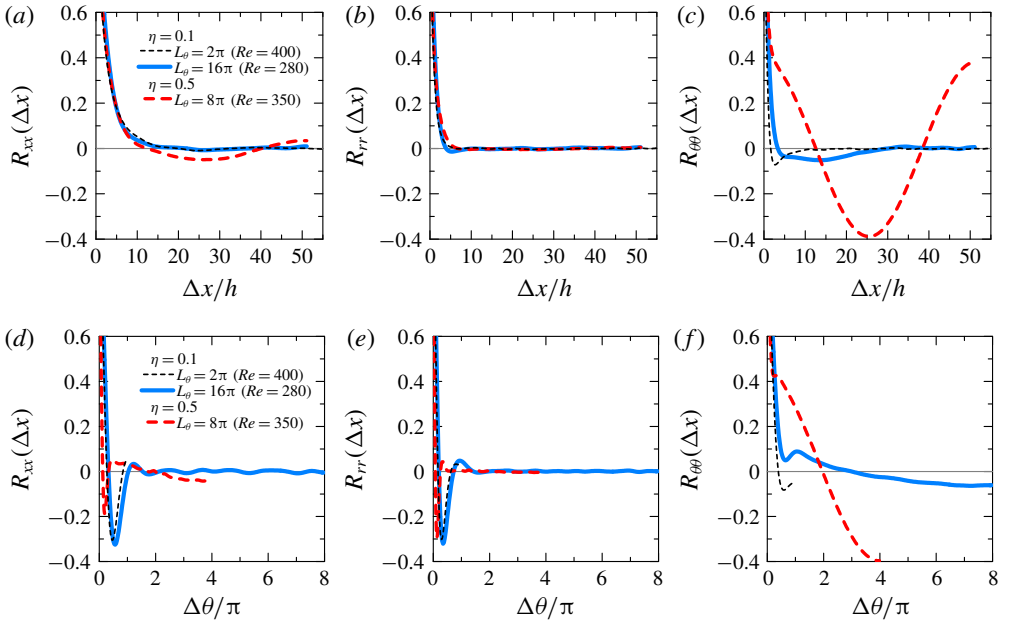


FIGURE 14. (Colour online) Two-point correlation of velocity fluctuations as a function of either an axial lag Δx (*a–c*) determined by (4.5) or an azimuthal lag $\Delta\theta$ (*d–f*) determined by (4.6): R_{xx} in (*a*,*d*), R_{rr} in (*b*,*e*) and $R_{\theta\theta}$ in (*c*,*f*) represent autocorrelations of u'_x, u'_r and u'_θ, respectively. The legend in (*a*) is also valid for (*b–f*).

puffs in pipe flow in the lower transitional regime ($Re = 2000$) display wider azimuthal correlations and longer streamwise correlations (Willis & Kerswell 2008).

These observations shed a new light on the regimes identified for $\eta = 0.1$, regardless of the choice of L_θ: as far as the azimuthal component is concerned, the transitional regime for $\eta = 0.1$ displays short-range correlations not found for the higher values of η investigated in this paper. The fact that the correlation decay is not modified between $L_\theta = 2\pi$ and 16π suggests that this regime is robust and not an artefact of either confinement by boundary conditions or of the artificial numerical extension in θ, though confirmation for even larger η would be welcome. A rapid comparison with the correlations found in aPf (Ishida *et al.* 2017), also close to the onset Reynolds number, confirms that they are all of the type encountered here for $\eta = 0.5$ and 0.8. The regime documented in § 3.3.2 is hence, to the best our knowledge, a new unreported regime of laminar–turbulent coexistence with short-range interactions between the turbulent fluctuations.

4.4. *Turbulent fraction*

The turbulent fraction $F_t(t)$ measures the instantaneous amount of turbulence in the flow independently of its local intensity. It is the natural way to quantify robust laminar–turbulent coexistence. If $F_t = 1$, the flow is turbulent everywhere, while $F_t = 0$ means that the flow is fully laminar. Figure 15 shows temporal averages of F_t, evaluated from x–z plane data evaluated at mid-gap. The local criterion for extracting laminar regions is based on thresholding the radial velocity: $|u'_r| < 0.015$ indicates locally laminar flow, while $|u'_r| > 0.015$ indicates locally turbulent flow. As shown

https://doi.org/10.1017/jfm.2019.666 Published online by Cambridge University Press

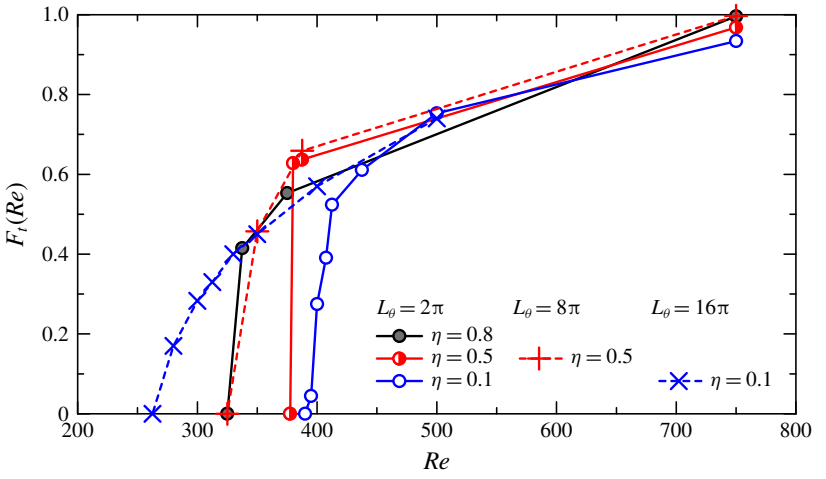


FIGURE 15. (Colour online) Time-averaged turbulent fraction F_t as a function of Re, nominal and artificially extended numerical domains with $L_\theta = 2\pi$, 8π and 16π.

in figure 15, for $Re = 750$, $F_t > 0.9$ for all values of η, when the flow can be unambiguously described as fully turbulent. The turbulent fraction F_t monotonically decreases on average as Re decreases, with a more significant decrease around $Re = 400$–500. For $\eta = 0.8$ and 0.1, localised turbulent structures (helical turbulence and turbulent puff, respectively) occur and then F_t approaches an average of 0.4. For $\eta = 0.5$, however, F_t directly jumps from 0.6 to 0 due to the lack of localised turbulent structure.

We focus then on the azimuthally extended systems. For $\eta = 0.5$ ($L_\theta = 8\pi$), helical turbulence occurs, but the slope of the curve $F_t(Re)$ and the pointwise values are directly comparable to the case $L_\theta = 2\pi$ above the critical point. Only the few additional non-zero values of F_t near the onset Reynolds number suggest a change in the curve of $F_t(Re)$, which can be linked to the release in azimuthal confinement. That change is compatible with continuous F_t even at the origin, although the trend cannot be confirmed at that stage. The situation becomes clearer for $\eta = 0.1$. For $\eta = 0.1$ ($L_\theta = 16\pi$), F_t shows values similar to the case $\eta = 0.1$ ($L_\theta = 2\pi$) when Re is in the range 400–750. However, below $Re = 400$, F_t displays a much smoother decrease from values of 0.3–0.4 down to zero for $Re \approx 275$ (the last non-zero point has in fact $F_t \approx 0.15$). This is where helical turbulence appears for $\eta = 0.8$ and $\eta = 0.5$ ($L_\theta = 8\pi$), whereas in our simulations for $\eta = 0.1$, intermittent patches of turbulence have not managed to self-organise into large-scale coherent structures.

5. Discussion

The numerical results from §§ 3 and 4 have revealed three different onset regimes depending on the value of η but also on the value of the numerical parameter L_θ:

(i) large-scale patterned turbulence at $\eta = 0.8$, similar to all the planar regimes described in the literature;

(ii) frustrated patterned turbulence at $\eta = 0.5$, similar to the previous regime but emergent in simulations only when the azimuthal confinement is released; and

(iii) a short-range laminar–turbulent coexistence regime at $\eta = 0.1$, with no oblique patterning even for artificially large values of L_θ, at least up to 16π.

https://doi.org/10.1017/jfm.2019.666 Published online by Cambridge University Press

The first regime has a direct equivalent in aPf above $\eta \geqslant 0.4$ and thus does not deserve a very long description. It is notorious from several recent studies that this regime, near its onset, is heavily influenced by finite-size effects both in numerical simulations and in experiments. As for the long-standing question as to whether the evolution of F_t with Re is continuous or discontinuous, the answer for the patterned regime clearly follows the answer given for all Couette-like flows: in 'affordable' numerical simulations, the transition at Re_g appears discontinuous (Bottin *et al.* 1998; Duguet *et al.* 2010*a*; Chantry, Tuckerman & Barkley 2017). However, in the thermodynamic limit (infinite extent in space and time) it is continuous, which implies well-defined scalings for several quantities asymptotically close to onset. Two such scalings can be considered here from our data: (i) the scaling of the turbulent fraction at equilibrium $F_t \sim \varepsilon^\beta$, where ε is the normalised distance to the onset, i.e. $\varepsilon = (Re - Re_g)/Re_g$, and (ii) the scaling in time of the unsteady turbulent fraction during relaminarisation $F_t(t) \sim t^{-\alpha}$. The consensus at the moment is that this transition in shear flows is continuous. Besides, it falls apparently into the universality class of directed percolation (DP), for which β and α only depend on the effective dimension of the problem (Lemoult *et al.* 2016; Sano & Tamai 2016; Chantry *et al.* 2017). In two spatial dimensions $\beta \approx 0.583$ and $\alpha \approx 0.451$, whereas in one spatial dimension $\beta \approx 0.276$ and $\alpha \approx 0.159$. A continuous transition also implies the divergence of most correlations at the onset Re_g. This unfortunately implies that the determination of Re_g itself, as well as that of exponents like β and α, also require divergent domain sizes and observation times, at the risk for the simulation or the experiment becoming rapidly unfeasible. In practice, however, the exponents are determined from finite-ε simulations in finite domains over finite observation times, provided the domain length is several times the correlation length (and similarly with time). In the patterning regime one can assume that the wavelength, for Re away from Re_g, yields a decent estimate of the correlation length; then the estimation of Re_g requires a domain size at least one order of magnitude times this wavelength. Given that the patterning wavelength for $\eta = 0.8$ and 0.5 is around $50h$ (cf. figures 4*b* and 6*b*), this suggests that no exponent can be trusted for sizes below $L_x \approx O(10^4)$, as confirmed in recent investigations of other shear flows (Lemoult *et al.* 2016; Chantry *et al.* 2017). Clearly this is beyond the present computational capacity for $\eta = 0.8$ and 0.5.

The discovery of a new regime for $\eta = 0.1$, with short-range correlations in all directions, changes the picture. The short correlation lengths reported in § 4.3 suggest that, from the point of view of the turbulent fluctuations, the numerical domain with $L_x \approx 200h$ is more 'extended', and in some sense closer to the thermodynamic limit of the related problem. We thus expect, for similar computational efforts as for other values of η, stronger evidence for continuous transition and easier measurements of the associated critical exponents. We thus replot the data for $\eta = 0.1$ from figure 15 in log–log coordinates in order to verify whether the scaling $F_t = O(\varepsilon^\beta)$ holds and, in case it does, which value β takes. This is displayed in figure 16 with $L_\theta = 16\pi$, and ε defined based on the choice $Re_g = 264$. The estimation of Re_g is performed classically by trial and error, checking that the curve $F_t(Re)$ displays algebraic decay/growth for the fitted value of $Re = Re_g$. A linear fit emerges over little less than a decade in F_t, which validates the notion of critical scaling. The fit for β is consistent with the theoretical value $\beta_{2D} \approx 0.583$ for DP in two spatial dimensions (but not with the exponent β_{1D}). Also plotted are the nominal cases of $L_\theta = 2\pi$ for $\eta = 0.1$ and 0.8, which exhibit, respectively, helically shaped and puff-like turbulence. Both plots are consistent with $\beta_{1D} \approx 0.276$ rather than 0.583 (although a steep slope that deviates from β_{1D} at $\varepsilon < 0.06$ might be due to shortage in the streamwise domain length). This

https://doi.org/10.1017/jfm.2019.666 Published online by Cambridge University Press

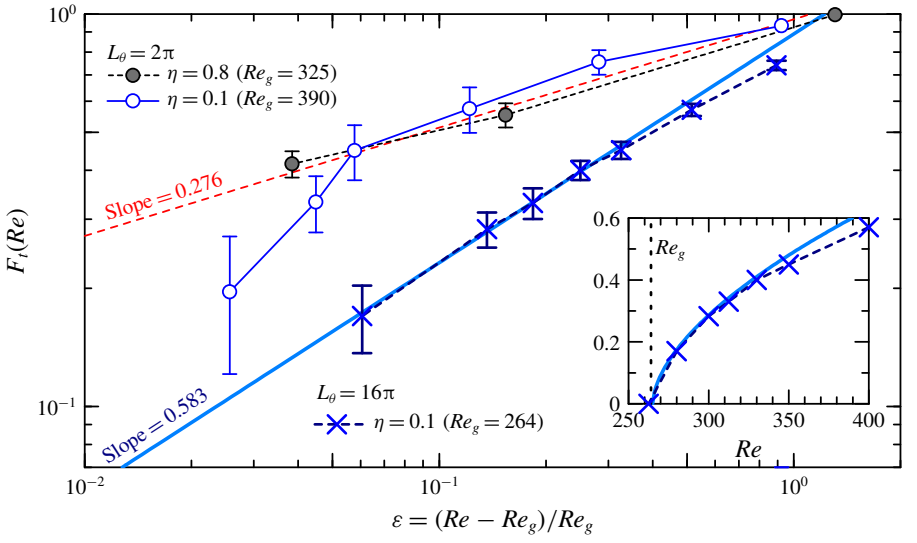


FIGURE 16. (Colour online) Critical behaviour of the turbulent fraction as a function of the normalised distance ε to the critical threshold Re_g (whose value is specific to each case), in log–log scale. The two straight lines represent power-law fits of the form $F_t \sim \varepsilon^\beta$ with $\beta_{2D} \approx 0.583$ as in $(2+1)$-DP (solid, blue online) and $\beta_{1D} \approx 0.276$ as in $(1+1)$-DP (dotted, red online). The inset shows the data for $\eta = 0.1$ with $L_\theta = 16\pi$ in linear scale as in figure 15.

alone is not sufficient to validate the $(2+1)$-DP picture of the new regime as two other independent exponents need to be validated as well. Among these exponents, we can have a rough approximation of the critical exponent α by monitoring in log–log plot the decay of $F_t(t)$ to laminar, starting from a noisy initial condition with finite F_t at $t = 0$. As can be seen in figure 17(*a*), the decay of an individual run for $Re \approx Re_g \approx 260$ alone cannot confirm the algebraic decay of F_t. There is always a possibility of obtaining an improved critical scaling range by choosing more specific initial conditions with higher turbulent fraction. Ensemble averaging over several such runs is, however, helpful since an unambiguously algebraic decay for $F_t(t)$ emerges over almost a decade in figure 17(*b*). The measured exponent is then consistent with the theoretical value of $\alpha_{2D} \approx 0.45$. The current data appear hence consistent with $(2+1)$-DP, though more data and more exponents would be needed to properly confirm this trend. Note in figure 17 that the scaling regime is reached after a relatively short time of $O(10h/u_w)$, especially compared with other similar studies (e.g. Lemoult *et al.* 2016; Chantry *et al.* 2017). This is consistent in order of magnitude with the shorter decay and splitting times observed in animations. This is another major advantage for gathering equivalent statistics compared to other flows displaying continuous transition.

By contrast, for the other cases $\eta = 0.8$ and 0.5 reported here, the numerical domain is so confined that no trend emerges: whatever the thermodynamic limit might be, the transition in that case only appears in practice as discontinuous. In other words, we have uncovered for $\eta = 0.1$ a new dynamical regime with short-range correlations, for which verification of the DP property seems computationally feasible using realistic domain sizes. This is in marked contrast to the majority of planar subcritical shear flows in which a similar task would still today appear as computationally hopeless.

https://doi.org/10.1017/jfm.2019.666 Published online by Cambridge University Press

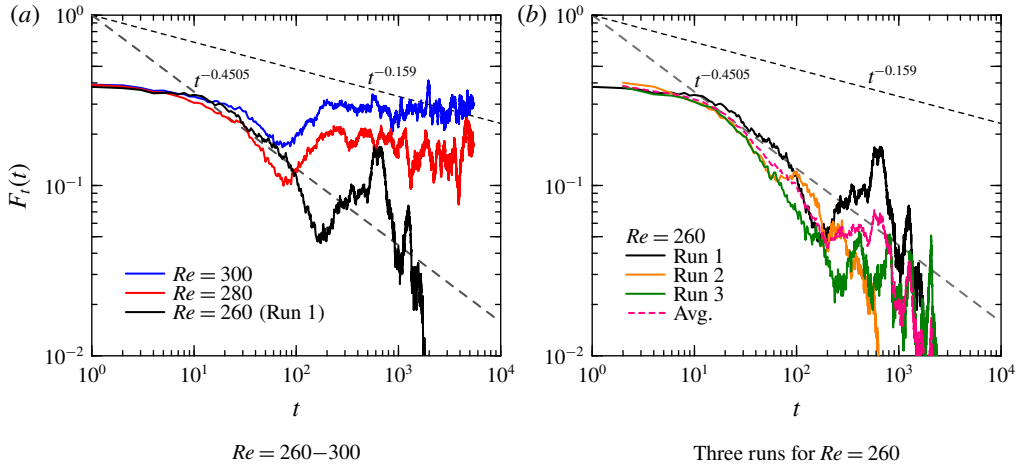


FIGURE 17. (Colour online) Instantaneous turbulent fraction $F_t(t)$ as a function of time for $\eta = 0.1$ and $L_\theta = 16\pi$ near the critical Reynolds number. Two dashed lines represent power laws of $F_t \propto t^{-\alpha}$ with the theoretical exponent of either $\alpha_{2D} = 0.4505$ for $(2+1)$-DP or $\alpha_{1D} = 0.159$ for $(1+1)$-DP.

6. Conclusion

Direct numerical simulation of aCf is reported using finite differences in long computational domains. The so-called transitional regimes of aCf, featuring coexistence of laminar and turbulent flow, have been investigated depending on the radius ratio η. The influence of an additional numerical parameter, the azimuthal L_θ (usually fixed to 2π), has also been considered as a way to question the direct influence of azimuthal confinement on the possible formation of large-scale flows and thus of organised laminar–turbulent coexistence. Three different regimes have been identified. For η close to unity (e.g. here 0.8) large-scale helical bands form as in the planar limit of pCf. For moderate η (e.g. here 0.5), these helical bands do not have enough space to form because of the azimuthal confinement. This is confirmed by their occurrence for L_θ sufficiently large with respect to 2π. Eventually, for low enough η, turbulence near its onset takes the form of disorganised patches; their localisation and interaction are reminiscent of turbulent puffs in pipe flow but their structure displays a strong asymmetry. Importantly, the correlation length between these puffs is shorter by one order of magnitude than the coherence length of organised patterns. This new regime appears as a potential candidate for DP, the short-range property even suggesting that critical exponents could be measured with significantly less computational effort than for the other long-range regimes usually encountered in subcritical shear flows. It remains an open question as to whether it is possible to identify other shear flow geometries in which turbulent patches would also display short-range correlations, preferably a realistic flow that can be released experimentally.

In this study, aCf has been introduced as a continuation prototype linking pCf to a one-dimensional flow geometry, with cylindrical pipe flow as the canonical example for a one-dimensional geometry. The present results indicate that high-η aCf connects smoothly with pCf, however it fails at connecting with the pipe flow for low η and is thus not a relevant candidate for this continuation. The presence of the inner rod, together with the no-slip condition on it, induces a mean flow differing strongly

https://doi.org/10.1017/jfm.2019.666 Published online by Cambridge University Press

from the one expected for a pipe flow. In particular, the statistics for $\eta = 0.1$ clearly demonstrate that, as for the laminar case, the highest shear is found near the inner rod, whereas the shear at the outer wall gets comparatively weaker as η is reduced. This corresponds to the opposite situation to pipe flow, where the shear is expected to vanish near the axis. The strong shear near the inner rod is responsible for the occurrence of a new dynamical regime characterised by short-range correlations and no large-scale organisation.

Acknowledgements

This work was supported by Grant-in-Aid for JSPS (Japan Society for the Promotion of Science) Fellowship 16H06066, 16H00813 and 19H02071. Numerical simulations were performed on SX-ACE supercomputers at the Cybermedia Centre of Osaka University and the Cyberscience Centre of Tohoku University.

Supplementary movie

Supplementary movie is available at https://doi.org/10.1017/jfm.2019.666.

REFERENCES

ABE, H., KAWAMURA, H. & MATSUO, Y. 2001 Direct numerical simulation of a fully developed turbulent channel flow with respect to the Reynolds number dependence. *J. Fluids Engng* **123** (2), 382–393.

ALFREDSSON, P. H. & MATSUBARA, M. 2000 Free-stream turbulence, streaky structures and transition in boundary layer flows. *AIAA Paper* 2000–2543.

AVILA, K., MOXEY, D., DE LOZAR, A., AVILA, M., BARKLEY, D. & HOF, B. 2011 The onset of turbulence in pipe flow. *Science* **333** (6039), 192–196.

BANDYOPADHYAY, P. R. 1986 Aspects of the equilibrium puff in transitional pipe flow. *J. Fluid Mech.* **163**, 439–458.

BARKLEY, D., SONG, B., MUKUND, V., LEMOULT, G., AVILA, M. & HOF, B. 2015 The rise of fully turbulent flow. *Nature* **526** (7574), 550–553.

BARKLEY, D. & TUCKERMAN, L. S. 2005 Computational study of turbulent laminar patterns in couette flow. *Phys. Rev. Lett.* **94** (1), 014502.

BARKLEY, D. & TUCKERMAN, L. S. 2007 Mean flow of turbulent–laminar patterns in plane Couette flow. *J. Fluid Mech.* **576**, 109–137.

BOTTIN, S., DAVIAUD, F., MANNEVILLE, P. & DAUCHOT, O. 1998 Discontinuous transition to spatiotemporal intermittency in plane Couette flow. *Europhys. Lett.* **43** (2), 171–176.

BRETHOUWER, G., DUGUET, Y. & SCHLATTER, P. 2012 Turbulent-laminar coexistence in wall flows with coriolis, buoyancy or Lorentz forces. *J. Fluid Mech.* **704**, 137–172.

CHANTRY, M., TUCKERMAN, L. S. & BARKLEY, D. 2017 Universal continuous transition to turbulence in a planar shear flow. *J. Fluid Mech.* **824**, R1.

COLES, D. 1965 Transition in circular Couette flow. *J. Fluid Mech.* **21** (3), 385–425.

DEGUCHI, K. & NAGATA, M. 2011 Bifurcations and instabilities in sliding Couette flow. *J. Fluid Mech.* **678**, 156–178.

DUGUET, Y. & SCHLATTER, P. 2013 Oblique laminar–turbulent interfaces in plane shear flows. *Phys. Rev. Lett.* **110** (3), 034502.

DUGUET, Y., SCHLATTER, P. & HENNINGSON, D. S. 2010*a* Formation of turbulent patterns near the onset of transition in plane Couette flow. *J. Fluid Mech.* **650**, 119–129.

DUGUET, Y., WILLIS, A. P. & KERSWELL, R. R. 2010*b* Slug genesis in cylindrical pipe flow. *J. Fluid Mech.* **663**, 180–208.

FAISST, H. & ECKHARDT, B. 2000 Transition from the Couette–Taylor system to the plane Couette system. *Phys. Rev.* E **61** (6), 7227.

https://doi.org/10.1017/jfm.2019.666 Published online by Cambridge University Press

FREI, C., LÜSCHER, P. & WINTERMANTEL, E. 2000 Thread-annular flow in vertical pipes. *J. Fluid Mech.* **410**, 185–210.

FUKUDOME, K. & IIDA, O. 2012 Large-scale flow structure in turbulent Poiseuille flows at low-Reynolds numbers. *J. Fluid Sci. Technol.* **7** (1), 181–195.

GITTLER, P. 1993 Stability of axial Poiseuille–Couette flow between concentric cylinders. *Acta Mech.* **101** (1–4), 1–13.

HOF, B., DE LOZAR, A., AVILA, M., TU, X. & SCHNEIDER, T. M. 2010 Eliminating turbulence in spatially intermittent flows. *Science* **327** (5972), 1491–1494.

HOF, B., WESTERWEEL, J., SCHNEIDER, T. M. & ECKHARDT, B. 2006 Finite lifetime of turbulence in shear flows. *Nature* **443** (7107), 59–62.

ISHIDA, T., DUGUET, Y. & TSUKAHARA, T. 2016 Transitional structures in annular Poiseuille flow depending on radius ratio. *J. Fluid Mech.* **794**, R2.

ISHIDA, T., DUGUET, Y. & TSUKAHARA, T. 2017 Turbulent bifurcations in intermittent shear flows: from puffs to oblique stripes. *Phys. Rev. Fluids* **2**, 073902.

LEMOULT, G., SHI, L., AVILA, K., JALIKOP, S. V., AVILA, M. & HOF, B. 2016 Directed percolation phase transition to sustained turbulence in Couette flow. *Nat. Phys.* **12**, 254–258.

LIU, R. & LIU, Q.-S. 2012 Non-modal stability in sliding Couette flow. *J. Fluid Mech.* **710**, 505–544.

NAGATA, M. 1990 Three-dimensional finite-amplitude solutions in plane Couette flow: bifurcation from infinity. *J. Fluid Mech.* **217**, 519–527.

ORSZAG, S. A. 1971 Accurate solution of the Orr–Sommerfeld stability equation. *J. Fluid Mech.* **50** (4), 689–703.

PRIGENT, A., GRÉGOIRE, G., CHATÉ, H., DAUCHOT, O. & VAN SAARLOOS, W. 2002 Large-scale finite-wavelength modulation within turbulent shear flows. *Phys. Rev. Lett.* **89** (1), 014501.

ROBERTSON, J. M. 1959 On turbulent plane-Couette flow. In *Proceedings of the Sixth Midwestern Conference on Fluid Mech.*, pp. 169–182. University of Austin, Texas.

SAMANTA, D., DE LOZAR, A. & HOF, B. 2011 Experimental investigation of laminar turbulent intermittency in pipe flow. *J. Fluid Mech.* **681**, 193–204.

SANO, M. & TAMAI, K. 2016 A universal transition to turbulence in channel flow. *Nat. Phys.* **12**, 249–253.

SCHMID, P. J. & HENNINGSON, D. S. 2001 *Stability and Transition in Shear Flows*, Applied Mathematical Sciences, vol. 142. Springer.

SEKI, D. & MATSUBARA, M. 2012 Experimental investigation of relaminarizing and transitional channel flows. *Phys. Fluids* **24** (12), 124102.

SHANDS, J., ALFREDSSON, P. H. & LINDGREN, E. R. 1980 Annular pipe flow subject to axial motion of the inner boundary. *Phys. Fluids* **23** (10), 2144–2145.

SHIMIZU, M. & KIDA, S. 2009 A driving mechanism of a turbulent puff in pipe flow. *Fluid Dyn. Res.* **41** (4), 045501.

SHIMIZU, M., MANNEVILLE, P., DUGUET, Y. & KAWAHARA, G. 2014 Splitting of a turbulent puff in pipe flow. *Fluid Dyn. Res.* **46** (6), 061403.

TSUKAHARA, T., KAWAGUCHI, Y., KAWAMURA, H., TILLMARK, N. & ALFREDSSON, P. H. 2010 Turbulence stripe in transitional channel flow with/without system rotation. In *Proceedings of Seventh IUTAM Symposium on Laminar–Turbulent Transition* (ed. P. Schlatter & D. S. Henningson), pp. 421–426. Springer.

TSUKAHARA, T., KAWAMURA, H. & SHINGAI, K. 2006 DNS of turbulent Couette flow with emphasis on the large-scale structure in the core region. *J. Turbul.* **7**, N19.

TSUKAHARA, T., SEKI, Y., KAWAMURA, H. & TOCHIO, D. 2005 DNS of turbulent channel flow at very low Reynolds numbers. In *Proceedings of the Fourth International Symposium on Turbulence and Shear Flow Phenomena, TSFP DIGITAL LIBRARY ONLINE* (ed. J. A. C. Humphrey *et al.*), pp. 935–940. Begel House Inc.

TSUKAHARA, T., TILLMARK, N. & ALFREDSSON, P. H. 2010*b* Flow regimes in a plane Couette flow with system rotation. *J. Fluid Mech.* **648**, 5–33.

WALTON, A. G. 2003 The nonlinear instability of thread–annular flow at high Reynolds number. *J. Fluid Mech.* **477**, 227–257.

https://doi.org/10.1017/jfm.2019.666 Published online by Cambridge University Press

WALTON, A. G. 2004 Stability of circular Poiseuille–Couette flow to axisymmetric disturbances. *J. Fluid Mech.* **500**, 169–210.

WALTON, A. G. 2005 The linear and nonlinear stability of thread-annular flow. *Phil. Trans. R. Soc. Lond.* A **363** (1830), 1223–1233.

WEBBER, M. 2008 Instability of thread-annular flow with small characteristic length to three-dimensional disturbances. *Phil. Trans. R. Soc. Lond.* A **464** (2091), 673–690.

WILLIS, A. P. & KERSWELL, R. R. 2008 Coherent structures in localized and global pipe turbulence. *Phys. Rev. Lett.* **100** (12), 124501.

WYGNANSKI, I. J. & CHAMPAGNE, F. H. 1973 On transition in a pipe. Part 1. The origin of puffs and slugs and the flow in a turbulent slug. *J. Fluid Mech.* **59** (2), 281–335.

WYGNANSKI, I., SOKOLOV, M. & FRIEDMAN, D. 1975 On transition in a pipe. Part 2. The equilibrium puff. *J. Fluid Mech.* **69** (2), 283–304.

https://doi.org/10.1017/jfm.2019.666 Published online by Cambridge University Press